


Entropy estimation within *in vitro* neural-astrocyte networks as a measure of development instabilityJacopo Teneggi *Department of Mechanical Engineering, Politecnico di Torino, Torino 10129, Italy;
Department of Physics, Georgetown University, Washington, District of Columbia, 20057, USA;
and Department of Biomedical Engineering, Johns Hopkins University, Baltimore, Maryland 21218, USA*

Xin Chen

*Department of Physics, Georgetown University, Washington, District of Columbia 20057, USA*Alan Balu *Department of Chemistry, Georgetown University, Washington, District of Columbia 20057, USA*Connor Barrett *Department of Physics, Georgetown University, Washington, District of Columbia 20057, USA*Giulia Grisolia and Umberto Lucia *Department of Energy “Galileo Ferraris,” Politecnico di Torino, Torino 10129, Italy*Rhonda Dzakpasu **Department of Physics, Georgetown University, Washington, District of Columbia 20057, USA
and Department of Pharmacology and Physiology, Georgetown University Medical Center, Washington, District of Columbia 20057, USA*

(Received 14 July 2020; revised 19 January 2021; accepted 1 March 2021; published 15 April 2021)

The brain demands a significant fraction of the energy budget in an organism; in humans, it accounts for 2% of the body mass, but utilizes 20% of the total energy metabolized. This is due to the large load required for information processing; spiking demands from neurons are high but are a key component to understanding brain functioning. Astrocytic brain cells contribute to the healthy functioning of brain circuits by mediating neuronal network energy and facilitating the formation and stabilization of synaptic connectivity. During development, spontaneous activity influences synaptic formation, shaping brain circuit construction, and adverse astrocyte mutations can lead to pathological processes impacting cognitive impairment due to inefficiencies in network spiking activity. We have developed a measure that quantifies information stability within *in vitro* networks consisting of mixed neural-astrocyte cells. Brain cells were harvested from mice with mutations to a gene associated with the strongest known genetic risk factor for Alzheimer’s disease, *APOE*. We calculate energy states of the networks and using these states, we present an entropy-based measure to assess changes in information stability over time. We show that during development, stability profiles of spontaneous network activity are modified by exogenous astrocytes and that network stability, in terms of the rate of change of entropy, is allele dependent.

DOI: [10.1103/PhysRevE.103.042412](https://doi.org/10.1103/PhysRevE.103.042412)**I. INTRODUCTION**

The brain is an energy intensive structure and must couple its ability to grow with the need to maintain stability [1]. Its flexibility to adapt to the environment must balance robustness against perturbations. Energy demands in the brain are high; it comprises only 2% of the human body mass, but consumes 20% of the total energy [2]. Brain energy requirements are dynamic as neuronal spiking activity drives energy consumption [3,4], and astrocytes, another class of cells in the brain, facilitate neuronal energy processing [5–7]. During development, a period when spontaneous activity is ubiquitous, energy considerations are vital. Anatomical circuitry is established in the

absence of modulating sensory input [8–13]. In addition, a large fraction of energy resources is utilized at the synapse, the site where spiking activity originates and information is conveyed from one cell to another; limits on the supply of energy will therefore influence information processing capacity. Indeed, the majority of energy consumption during development is attributed to synaptic synthesis and efficacy, which promotes brain circuitry development [14–16]. Energy demands mediate network driven oscillations [17] and require that information transmission is maximized at minimum energy cost.

Coordinated spontaneous activity during development has been widely studied in several structures such as the retina, spinal cord, neocortex, and hippocampus, as it serves to create a template for healthy circuit development capable of respond-

*Corresponding author: rhonda.dzakpasu@georgetown.edu

ing to subsequent sensory input [18–22]. This development is strongly influenced by the ability of the circuit to efficiently process and transmit neural information and energy [23]. While it is important to quantify information transmission, experimental constraints in measuring intracellular spiking dynamics limit the ability to determine a relationship between information transmission and network development instability. Network scale intracellular recording methods are required and currently such methods are limited to simultaneous recordings from only a few neurons [24]. As such, it is necessary to develop quantitative measures to serve as indirect proxies for information transmission, such as entropy.

We describe a suite of analytical tools designed to assess time-dependent changes of spiking dynamics within neuronal networks. On the cellular level, synchronous activity affects the probability of postsynaptic firing, as in long-term potentiation [25–28] and collective activity on the network level influences information transmission [29–35]. Information theoretic measures have been used to infer a wide range of phenomena associated with collective dynamics, in experimental and computational systems [19,20,36–46]. For example, Meshulam *et al.* [42] implemented a theoretical framework to create a maximum entropy model from *in vivo* population recordings of hippocampal CA1 neurons. Their model accurately predicted neuronal activity regardless of the cell’s ability to code for position. In a computational model, mutual information (MI) was used to calculate the relationship between the MI of a network of stochastic units that code for a particular stimulus and their distance from the response probabilities induced by continuous or discrete stimuli [38]. They showed a logarithmic relationship when the stimulus was continuous and an exponential one for a discrete stimulus suggesting that MI is a useful tool to measure neural codes.

Here, we quantify energy across the network as a function of the spiking neuronal activity in time bins within a recording epoch; we define the entropy of the system using these energy states. Based upon these quantities, we devise a metric to evaluate the stability of developing networks. Dysfunction in spiking activity during development can cause severe alterations in synaptic connectivity and neurodevelopmental disorders [2,47], resulting in network instabilities; however, such instabilities might not appear until later in the lifetime of the organism. We apply this measure to evaluate spontaneous dynamics from developing networks of *in vitro* hippocampal neurons and astrocytes. Cells were harvested from the brains of mice in which mutations were made to the gene associated with the strongest genetic risk factor for Alzheimer’s disease, *APOE*.

Apolipoprotein E (APOE), the protein associated with the *APOE* gene, is a lipid transport protein primarily produced by astrocyte cells in the brain [48,49]. It is thought to be involved in neuronal repair after injury [50–52]. There are three major *APOE* mutations: *APOE2* is believed to be protective, *APOE3* is neutral, and *APOE4* dramatically increases risk for developing Alzheimer’s and decreases the age of onset in a gene-dose-dependent manner [50,53]. We show that in networks composed of neurons and astrocytes harvested from *APOE4* mice, and in networks consisting of neurons and astrocytes harvested from mice that do not make APOE, the development profiles are unstable, but in opposing manners.

However, networks of neurons and astrocytes harvested from *APOE2* mice are shown to be stable. Similar trends were also measured from networks of neurons harvested from mice that do not make APOE, but were supplemented with astrocytes from mice that produce either *APOE2* or *APOE4*.

This paper is organized as follows. In Sec. II, we describe the experimental design and detail the quantitative measures. In Sec. III, we describe the physiological phenomena that we observed in the extracellular membrane potential fluctuations within each network. We apply our measures of energy and entropy to these neural-astrocyte networks as a function of time to characterize their differences. Finally, in Sec. IV, we discuss our findings.

II. METHODOLOGY

A. Experiment

Animal protocols conformed to NIH guidelines and approved by the Georgetown University Animal Care and Use Committee were used. Please refer to Appendix A for cell culturing details. Briefly, single cell suspensions of embryonic hippocampal neurons were separately harvested from the following types of *APOE* mice and plated onto previously prepared microelectrode arrays (MEAs): mice that do not make APOE (*APOE KO*), *APOE2* mice, and *APOE4* mice. Astrocytes from *APOE2* and *APOE4* targeted replacement mice were provided as a gift from the G. W. Rebeck laboratory. On day *in vitro* 7 (DIV7), astrocytes from either *APOE2* or *APOE4* mice were added to MEAs plated with *APOE KO* neurons to achieve an astrocyte to neuron ratio of 0.4. Control *APOE-KO* networks contained no exogenous astrocytes. No additional astrocytes were added to MEAs that contained hippocampal neurons harvested from *APOE2* or *APOE4* mice, i.e., the endogenous astrocytes synthesizing either *APOE2* or *APOE4*, respectively. To ensure reproducibility of results across animals, all reported experimental groups were derived from multiple experimental preparations.

Figure 1 shows the sequence of recording and preprocessing of the MEA data. We recorded all spontaneous electrical activity using the MEA2100 amplifier, A0, residing on a heated microscope stage at 37°C. The MEA is composed of 59 TiN electrodes, each of which is 30 μm in diameter and arranged on an 8 × 8 square array. In addition, there is one reference electrode and four auxiliary analog channels; the interelectrode spacing is 200 μm. Electrical activity is amplified and sampled at a 10 kHz acquisition rate in order to allow the detection of spikes. To assess the development of each network, 5-min recordings began on DIV10 and continued daily until DIV21. Data were digitized and stored on a Dell personal computer (Round Rock, TX) for offline analysis.

Low-frequency components were removed by high-pass filtering all MEA voltage traces at 25 Hz (MCRack, Multi Channel Systems MCS GmbH, Reutlingen, Germany). Negative voltage deflections were observed during recordings and these recorded spikes were detected using a threshold algorithm from Offline Sorter (Plexon Inc., Dallas TX). Spikes were calculated as a multiple of the standard deviation of the biological noise ranging between $\pm 6\sigma$ and $\pm 7\sigma$. As described below, we used custom software written in MATLAB (The

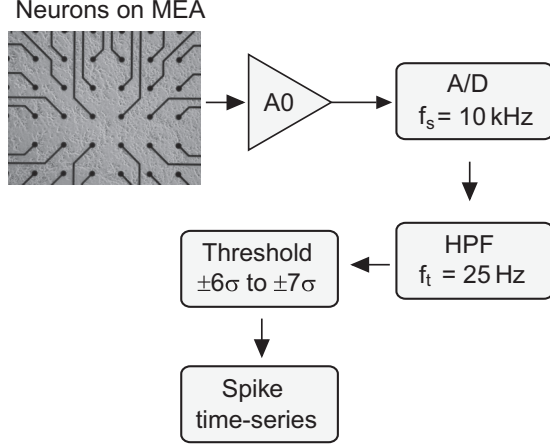


FIG. 1. Schematic of the recording and filtering system. Neurons and astrocytes are plated onto an MEA. The extracellular voltage signal is amplified using the integrated signal processor and headstage of the MEA2100 system. To reliably capture extracellular action potentials, data is sampled to the computer at 10 kHz. Spike times are extracted using a second-order Butterworth high-pass filter at 25 Hz.

Math Works, Natick, MA) to analyze the activity from the mixed hippocampal neural-astrocyte cell networks.

B. Data analysis

1. Binning

Figure 2 outlines the analysis process. Let $T = (t_1, t_2, \dots, t_n)$ be the spike time series for an electrode, where t_n is the time of occurrence of a spike; we pick a bin size τ with which to divide the recording epoch. So, $N_\tau = 300/\tau$ is the number of bins.

We compute the binary vector $B \in [0, 1]^{N_\tau}$ such that

$$b_i = \begin{cases} 1, & \text{if } \exists t \in T : (i-1)\tau \leq t < i\tau \\ 0, & \text{otherwise.} \end{cases} \quad (1)$$

That is, b_i is 1 if there is at least one spike in the i th time bin. The binning process returns the binary matrix $M \in \{0, 1\}^{N_\tau \times N_\tau}$, where N_τ is the number of active electrodes in each MEA. We use three physiologically relevant bin sizes: 3, 10, and 100 ms, which resulted in 1×10^5 , 3×10^4 , and 3×10^3 data points per DIV per electrode, respectively.

2. Energy estimation

There are many approaches to encoding energy within neurons and neural networks [54]. We base our method on [42] and estimate the energy state of each network using the number of electrodes that are simultaneously active in each bin.

Let $E = (e_1, e_2, \dots, e_{N_\tau})$ be the normalized energy vector such that

$$e_i = \frac{\sum_{j=1}^{N_\tau} M_{ij}}{N_\tau}. \quad (2)$$

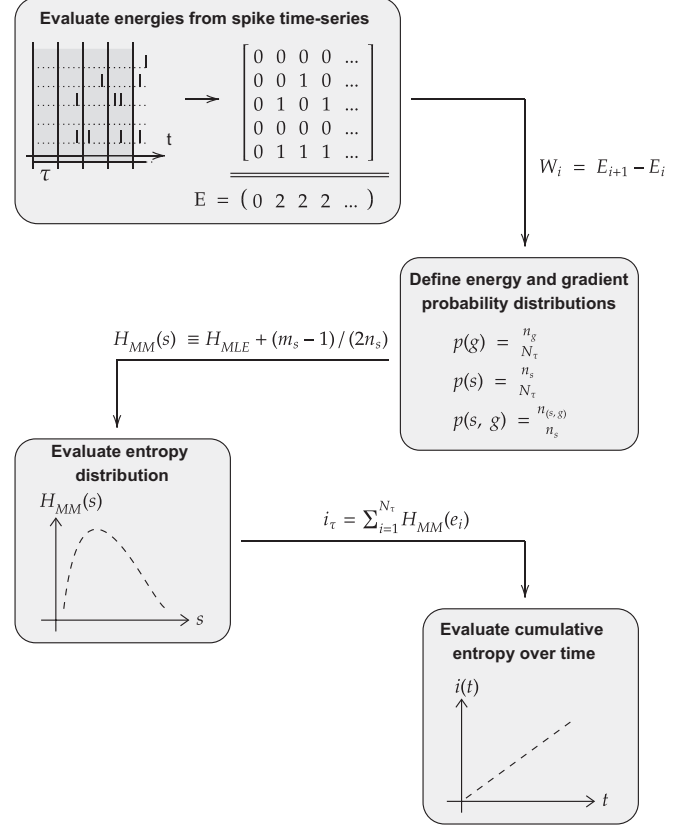


FIG. 2. Overview of the data analysis process.

e_i is a discrete variable that can assume a finite set of values, \mathcal{S} :

$$\mathcal{S} = (0, 1, \dots, N_\tau) \frac{1}{N_\tau}. \quad (3)$$

To determine how the energy states are distributed in each network, we estimate their probability distribution,

$$\hat{p}(s) = \frac{n_s}{N_\tau}, \quad (4)$$

where n_s is the number of occurrences of the energetic state s in the energy vector E .

Let $W = (w_1, \dots, w_i, \dots, w_{N_\tau-1})$ be the energy gradient vector where

$$w_i = e_{i+1} - e_i. \quad (5)$$

w_i is a discrete variable that can assume a finite set of values, \mathcal{G} :

$$\mathcal{G} = (-N_\tau, \dots, -1, 0, 1, \dots, N_\tau) \frac{1}{N_\tau}. \quad (6)$$

We fit the raw energy distributions from the set of MEAs with the same allele on the same DIV to a generalized decreasing sigmoid

$$f(x; a) = a_1 [1 - (1 + a_2 e^{-a_3 x})^{-1/a_4}], \quad (7)$$

using the penalized loss function

$$l(x; a) = f(x; a) - y + \lambda \|a\|. \quad (8)$$

Here, we have

$$\begin{aligned} x &= \ln [\widehat{p}(S)], \\ y &= S, \end{aligned} \quad (9)$$

where S is the concatenation of the energy state vectors E from each MEA and $\widehat{p}(S)$ is their probability. We use MATLAB's `lsqnonlin` function [55,56] that implements a trust-region-reflective algorithm based on the interior-reflective Newton method described in [57,58]. We train the learned parameters a on 70% of S and we test on the remaining 30% and choose the value of λ that minimizes the loss function.

3. Entropy estimation

We define the discrete phase space Ω such that

$$\Omega = \{(s, g), s \in \mathcal{S}, g \in \mathcal{G}\} \quad (10)$$

and

$$\widehat{p}(s, g) = \frac{n_{(s, g)}}{N_\tau}, \quad (11)$$

where $n_{(s, g)}$ is the number of occurrences of the point (s, g) . Then, we estimate the conditional probability:

$$\widetilde{p}(s, g) = \frac{\widehat{p}(s, g)}{\widehat{p}(s)} = \frac{n_{(s, g)}}{n_s}, \quad (12)$$

such that

$$\sum_{g \in \mathcal{G}} \widetilde{p}(s, g) = 1. \quad (13)$$

In order to estimate the entropy of each energetic state s we use Miller's [59] estimator (see Appendix B), defined as

$$\widehat{H}_{\text{MM}}(s) \equiv \widehat{H}_{\text{MLE}} + \frac{m_s - 1}{2n_s}, \quad (14)$$

where \widehat{H}_{MLE} is the maximum likelihood estimator of Shannon's entropy [60], such that

$$\widehat{H}_{\text{MLE}} = - \sum_{g \in \mathcal{G}} \widetilde{p}(s, g) \log_2 \widetilde{p}(s, g), \quad (15)$$

and $m_s = \#\{g : \widetilde{p}(s, g) \neq 0\}$.

We fit the raw entropy distributions from all MEAs from the same treatment on the same DIV to a fourth-degree polynomial using MATLAB's `polyfit` function [55].

Finally, we estimate the expected value of the entropy

$$E[H] = \sum_{s \in \mathcal{S}} p(s)H(s) \quad (16)$$

with the mean entropy

$$\begin{aligned} m &= \sum_{s \in \mathcal{S}} \widehat{p}(s) \widehat{H}_{\text{MM}}(s) \\ &= \frac{1}{N_\tau} \sum_{i=1}^{N_\tau} \widehat{H}_{\text{MM}}(e_i) \\ &= \frac{i_\tau}{N_\tau}. \end{aligned} \quad (17)$$

To investigate the evolution of the mean entropy over development, we define the relative entropy as

$$m(dB) = 20 \ln \left(\frac{m_{\text{DIV}x}}{m_{\text{DIV}10}} \right), \quad (18)$$

where $x \in \{14, 18, 21\}$.

III. RESULTS

Embryonic neurons were plated onto previously prepared MEA substrates as depicted in Fig. 1. To reflect changes in development stability of the networks, we analyzed datasets from four time points within a 12-day period between DIV10 and DIV21. Rastergrams of spontaneous activity from *APOE-KO* neurons plated with or without exogenous astrocytes are presented in Fig. 3 and from mixed neural-astrocyte *APOE2* and *APOE4* networks in Fig. 4. Figure 3(a) shows that in the absence of APOE, network activity is sparse, with little increase in spiking over time. In contrast, *APOE-KO* neurons that were supplemented with either *APOE2* [Fig. 3(b)] or *APOE4* [Fig. 3(c)] astrocytes display more activity as early as 3 days after the addition of exogenous astrocytes; these networks continue to develop resulting in strong, robust firing patterns by DIV21. In Fig. 4, endogenous astrocytes in these networks synthesize either *APOE2* [Fig. 4(a)] or *APOE4* [Fig. 4(b)], respectively. Activity was robust early in development on DIV10. By DIV21, *APOE2* networks display uniform, synchronous activity whereas the *APOE4* networks have a broader range of firing patterns. Several electrodes display high-frequency firing patterns whereas activity in other electrodes is very sparse.

We calculate the energy distribution within each network during the course of their development. Figure 5 shows the evolution from DIV10 to DIV21 of the fits to the energy distributions for $\tau = 10$ ms. We refer the reader to the raw data plots in Appendix E, Fig. 11. The macroenergy state is normalized to a number between 0 and 1, where 0 corresponds to the absence of activity within a bin across all electrodes, and 1 corresponds to activity in all possible channels for a given bin, i.e., an ideally synchronous network state. The learned parameters of the fits are not used in any quantitative evaluation; importantly, the artifact at $\widehat{p}(e) = 1$ for $e \sim 0$ should be disregarded.

One feature common to all four networks is that the quiescent state, i.e., $e = 0$, is the most probable network state regardless of the developmental state of the network (Fig. 6). This quiescent state probability is very high throughout the development of all networks and is quite stable for both $\tau = 3$ ms [Fig. 6(a)] and 10 ms [Fig. 6(b)]. When $\tau = 100$ ms [Fig. 6(c)], the quiescent state is still the most probable state, but its value decreases considerably. Additionally, there are large fluctuations in the *APOE4* networks; the quiescent state probability drops considerably on DIV18 with minimal recovery on DIV21. However, once $e > 0$, activity patterns between the networks begin to differentiate over time (Fig. 5).

On DIV10 [Fig. 5(a)], *APOE2* networks and both *APOE-KO* networks are quite similar; as the energy state increases, the probability gradually decreases. In the *APOE4* networks,

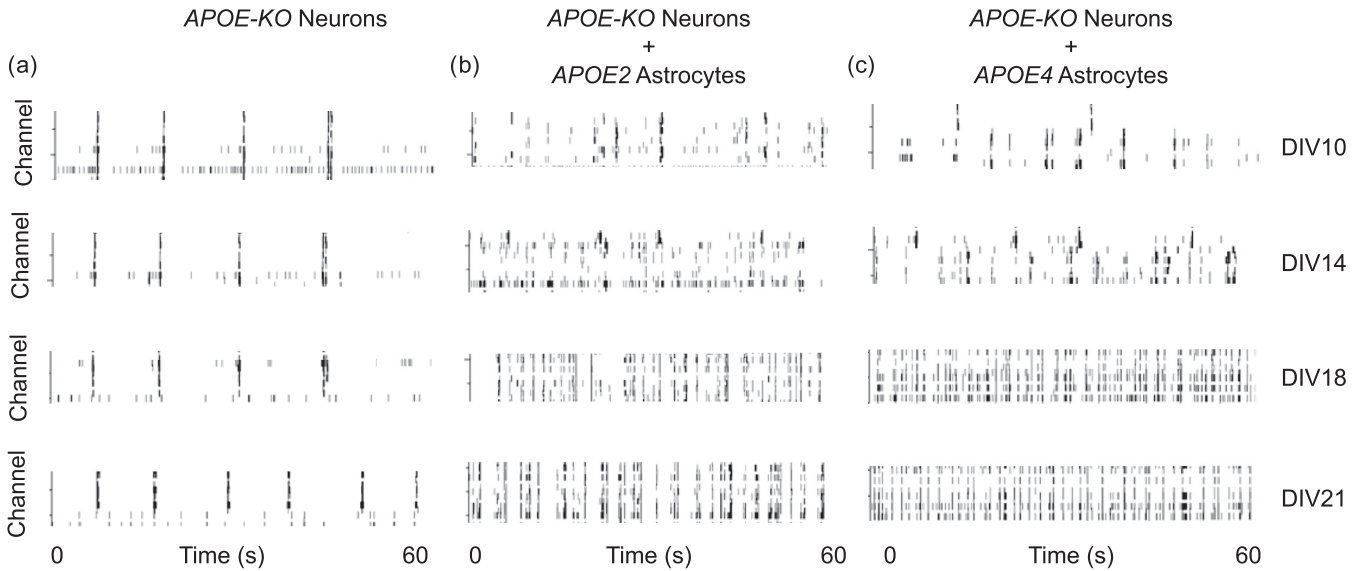


FIG. 3. Rastergrams of 1 min of network activity from several channels in *APOE-KO* neural networks under the different experimental conditions show qualitative changes in spiking dynamics as the networks develop. (a) Networks with no exogenous astrocytes display sporadic synchronized spiking on DIV10. The synchronous activity does not become uniform or more widespread as the activity evolves. (b) Astrocytes from *APOE2* mice were added on DIV7. By DIV10, 3 days after the addition, activity has increased and by DIV21, there are several synchronized electrodes. (c) Astrocytes from *APOE4* mice were added on DIV7. On DIV10, there are clusters of increased activity. By DIV21, as in panel (b), activity has increased with uniform firing throughout the epoch.

there is a sharp drop in the probability when $e > 0$ and the range of energy states is not as broad. On DIV14 [Fig. 5(b)] the range of occupied energy states increases for all four networks ($e_{\max} \sim 0.7$) compared to DIV10 ($e_{\max} \sim 0.5$). We remark that a higher energy corresponds to more simultaneously active electrodes and therefore all networks increase their synchronicity at this time. It is also interesting to note that both KO networks show an inflection point, while the

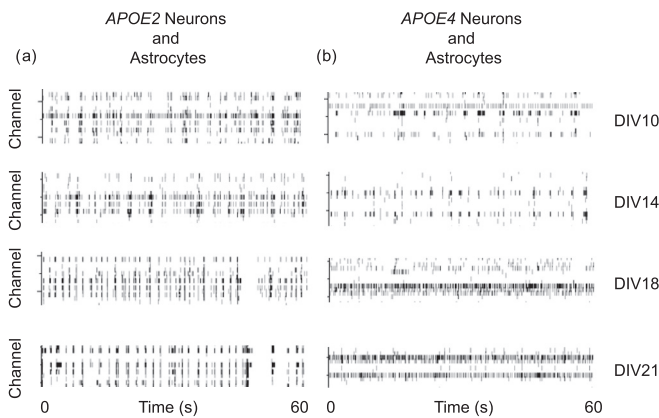


FIG. 4. Rastergrams of 1 min of network activity from several channels in the *APOE2* and *APOE4* networks show qualitative changes in spiking dynamics as the networks develop. (a) *APOE2* networks display a modest transition to synchrony by DIV21. (b) *APOE4* networks have a wide range of activity patterns and by DIV21, there are electrodes exhibiting very sparse firing and others with persistent activity.

APOE4 networks maintain the same concavity throughout their development.

On DIV18 [Fig. 5(c)], both *APOE-KO* networks strongly overlap as well as increase to a higher maximum energetic state ($e_{\max} \sim 0.8$); there is also a broad, flat region of states with equal probability, indicating a nearly uniform energy distribution at this point in their network development. In contrast, the distributions in the *APOE4* networks have their broadest range of energies on DIV14 and start to contract by DIV18 ($e_{\max} \sim 0.55$). The *APOE2* networks have a consistent profile from DIV14 to DIV18. Lastly, on DIV21 [Fig. 5(d)], both *APOE-KO* networks are stable from DIV18, with a maximum energy state near $e_{\max} \sim 0.8$. *APOE4* networks are stable from DIV18 to DIV21, while *APOE2* networks have a small increase in their energy range with the emergence of a small inflection point.

These energy distributions provide a picture of the evolution of global activity and synchronicity during the development of each network. Next, we ask how likely during the recording epoch, does each network transition between energy states. Given that a network is in a particular energy state, what is the probability that it will increase or decrease its energy?

To investigate these questions we define the energy gradient w as the difference between two consecutive energetic states: $w > 0$ indicates increasing energy, $w < 0$ indicates decreasing energy, and $w = 0$ indicates a steady state. We evaluate energy gradients within each recording epoch and calculate the conditional probability distributions. This results in phase-space plots of energy gradients that describe the cal-

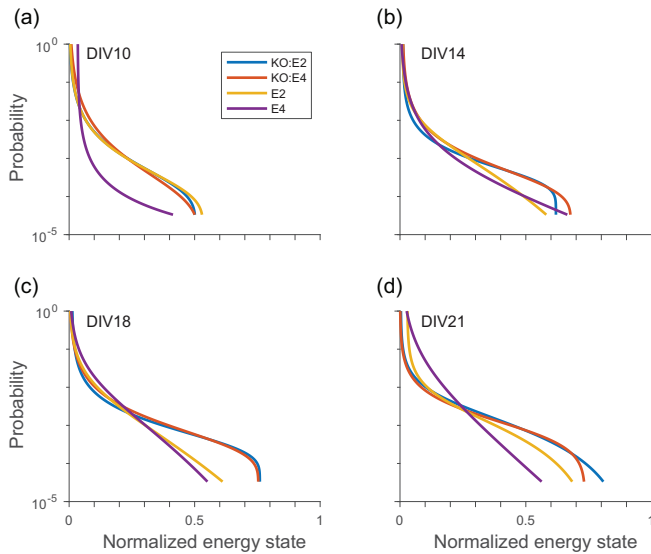


FIG. 5. Energy distribution sigmoid fits for $\tau = 10$ ms during network development. (a) On DIV10, both *APOE-KO* and *APOE2* show a similar profile; as the energy states increase, there is a gradual decrease in the probability. *APOE4* networks have a sharp drop in probability as the energy increases. (b) On DIV14, the *APOE-KO* networks have a small increase in their maximum energy state. The sharp drop in the *APOE4* profile from DIV10 has decreased and these networks expand their range of energy states. The *APOE2* networks are similar to their DIV10 profile with a small reduction in the slope. (c) *APOE-KO* networks overlap in their energy profile with a maximum in their energy state of 0.8. *APOE2* networks are nearly constant from DIV14 and *APOE4* networks start to contract their energy profile. (d) All networks remain nearly the same as for DIV18.

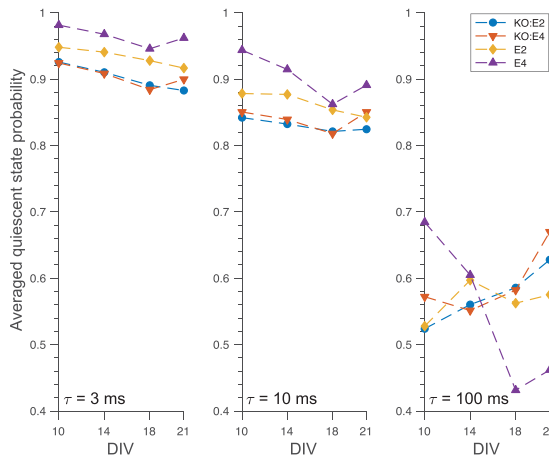


FIG. 6. Average quiescent state probabilities. (a) When $\tau = 3$ ms, all networks have a very high probability with little fluctuation during network development. (b) There is a small drop in the overall probability for $\tau = 10$ ms. Developmental variability is small for all networks, with the exception of *APOE4* networks having an increase in fluctuations on DIV18. (c) When $\tau = 100$ ms the probability of the quiescent state drops for all networks and there is a large drop for *APOE4* networks from DIV10 to DIV18. Fluctuations in the other networks remain small.

culated moves from energy states within each network, akin to the moves within a chess game.

Figure 7 shows the conditional probability distributions of the energy gradient plots, $\tilde{P}(e, w)$, of four representative MEAs: one per *APOE* treatment. Within each spatial map, we identify four different regions, which vary in extent and sparsity depending on the type of astrocytes that are present in each neuronal network. A bright-red region is bounded by the $w = 0$ and the $w = -e$ diagonal (i.e., return to $e = 0$). This triangular region shows the high probability that a network will decrease rather than increase its energy. A slim, blue-green arch extending upwards from the origin describes the transition probabilities to higher energy states and shows the paths networks take to generate events that will lead to bursts. Cells along the leftmost column, ($e = 0, w \in \mathcal{G}$), have a greater probability to experience energy increases in an incremental, stepwise fashion rather than taking large jumps. In general, for any nonzero energy state, as the energy increases, it is more likely that the system will decrease in energy (red regions) and the higher the energy, the harder, i.e., lower probability, it is for the network to increase its energy. The outer regions where dark blue predominates are regions in the phase space for which there are no observed transitions in energy.

Early in the development on DIV10, all networks start with a small fraction of the phase space occupied, with the *APOE4* network occupying a particularly small fraction of phase space. For all networks, regions with higher probability consist primarily of transitions to lower energy states; in general, there are few states with a nonzero probability to transition to a higher energy state. On DIV14, most of the networks continue to have many areas defined by high probability transitions to lower energy states. The *APOE4* network [Fig. 7(d)] also has regions with high transition probabilities to higher energy states. In addition, all of its high probability transitions are surrounded by areas with zero probability. On DIV18, the occupied phase space increases for all networks except for the *APOE4*. The *APOE-KO-E2* network [Fig. 7(a)] has several sites with high transition probabilities to lower energies and the gradients are large, ranging from 0.2 to 0.4. Interestingly, these accessible states are also interspersed with many zero-probability transitions. Also, there is a cluster of high-probability states with transitions from lower to higher energies, but they are not prevalent until DIV18 and the initial states with these high probabilities are around 0.4. For the *APOE-KO-E4* network [Fig. 7(b)], there are fewer inaccessible transitions surrounding accessible transitions. In addition, the transition probabilities to lower energy states are not as high as in the *APOE-KO-E2* network. The *APOE2* network [Fig. 7(c)] does not have many accessible transitions at high energies. The phase space for the *APOE4* [Fig. 7(d)] network reverts to a similar structure of few accessible states as seen on DIV10. Both the *APOE-KO-E2* and *APOE-KO-E4* networks have stable patterns from DIV18 to DIV21. For the *APOE2* network, the general phase-space boundary is similar from DIV18 to DIV21, with a slight increase in the number of high-probability transitions. As with the *APOE-KO-E2* network, these transitions are interspersed with regions of zero probability. Finally, while there is an expansion in the phase space for the *APOE4* network from DIV18 to DIV21, the

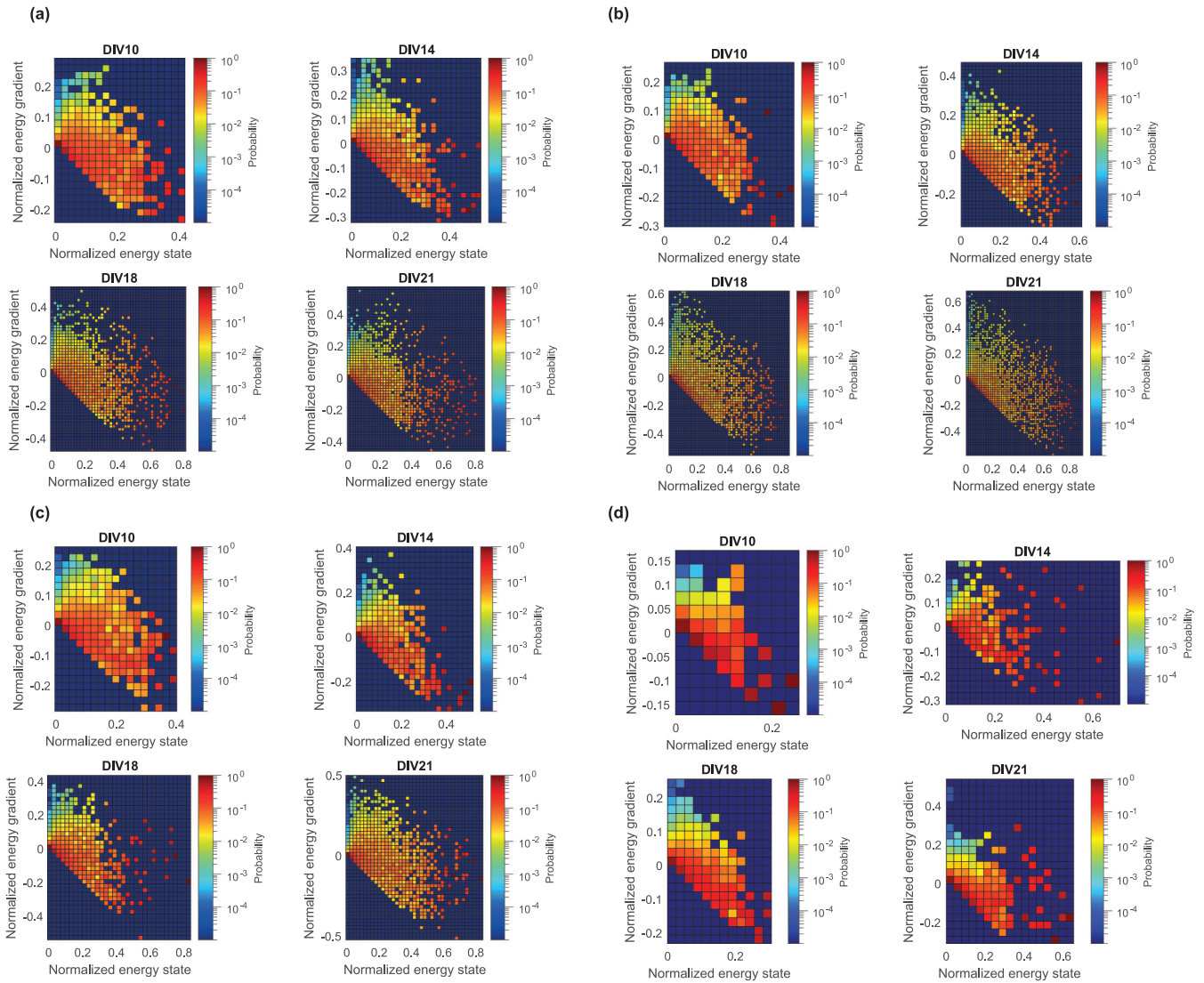


FIG. 7. Representative phase-space maps of conditional probabilities for the energy gradient at $\tau = 10$ ms during network development. Overall, most of the occupied areas have a high probability to transition to a lower energy state. (a) For the *APOE-KO-E2* networks on DIV10, the transitions with high probability typically have small gradients, clustered around zero; on DIV14, the gradients increase for the regions with high-probability transitions to lower energies. By DIV21, more of the phase space is occupied, with a prominent speckle pattern of high transition probabilities. (b) *APOE-KO-E4* networks follow a similar trajectory as the *APOE-KO-E2* networks for DIV10 and DIV14. By DIV18 and DIV21, transition probabilities to lower energy states are high when the initial energy state is high. There are also more nonzero probability transitions, creating a smoother pattern of accessible states. (c) *APOE2* networks also have a similar clustering of high transition probabilities with small gradients on DIV10. On DIV14, the high-probability transitions to lower energy states tend to occur with larger gradients. When the network is in a high energy state by DIV18, transitions to lower energy states are sparse and by DIV21, high-probability transitions to lower energy states increases, with an emerging speckle pattern due to regions of zero probability transitions. (d) *APOE4* networks start with the smallest occupied region of phase space and the occupied region increases on DIV14; high-probability transitions increase. Interestingly, these high-probability transitions originate from a high or low energy state; these transitions are surrounded by large regions of zero-probability transitions. By DIV21, the map expands to higher energies with large transition probabilities, with a lower density than that of the other networks.

high-probability transitions at the higher energy states are surrounded by many inaccessible regions.

To account for experimental variability, we normalize m , the mean entropy, over the number of active electrodes in the experiment to obtain the mean single-electrode entropy, $m_r \equiv m/N_{\text{active}}$ (we refer the reader to Fig. 12 in Appendix E for

the raw entropy distributions as a function of energetic state). Figure 8 shows the fits for the cumulative single-electrode entropies by different networks on different DIVs, as a function of the duration within each recording epoch. *APOE4* networks are the least stable, with a strong increase of mean entropy over DIV, whereas the *APOE2* networks display a consistent

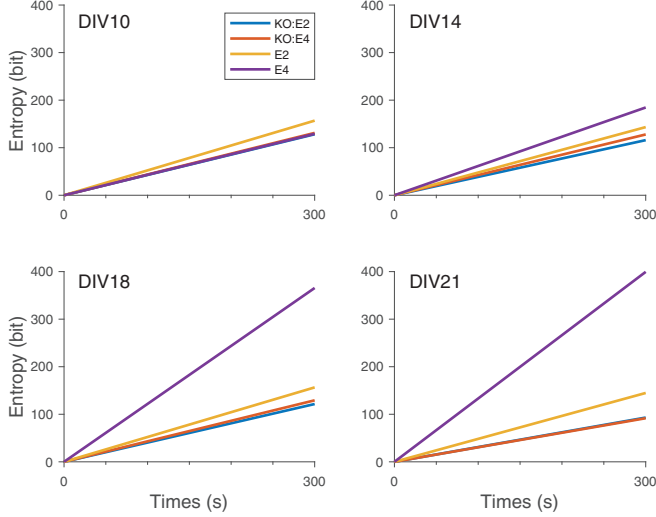


FIG. 8. Cumulative entropy linear fits as a function of time for $\tau = 10$ ms. On DIV10, the cumulative entropy is nearly the same for all networks. From DIV14 through DIV21, *APOE4* networks have the largest cumulative entropy. *APOE2* networks show a steady and consistent value in their cumulative entropy during development. Both *APOE-KO* networks show the smallest change in their cumulative entropy during development.

pattern during development. *APOE-KO-E2* and *APOE-KO-E4* networks display similar, largely overlapping, trajectories.

Figure 9 shows the mean single-electrode relative entropies for all taus during the course of network development. Here, we include the mean relative entropies for the *APOE-KO* control networks (i.e., networks with no additional astrocytes) to evaluate how the addition of astrocytes to neuronal networks from *APOE-KO* mice affects stability. Interestingly, the entropy in the *APOE-KO* control networks decrease exponentially for $\tau = 10$ and 100 ms, albeit with large fluctuations from DIV10 to DIV14. In contrast, the entropy in the *APOE4*

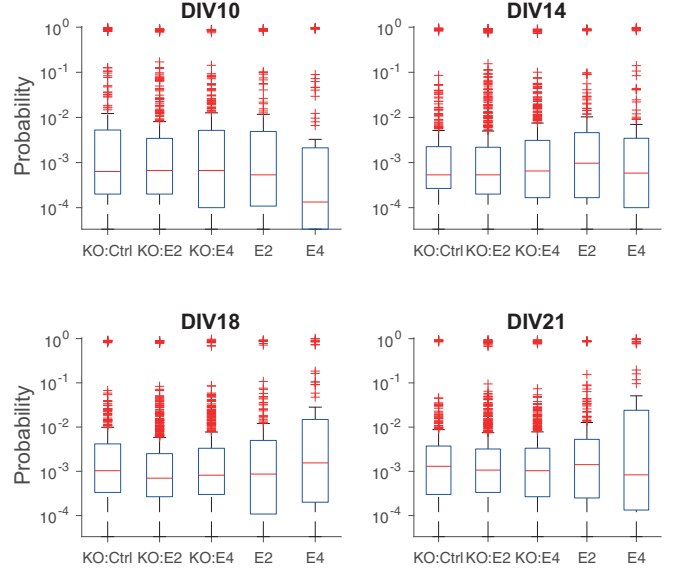


FIG. 10. Distributions of $\hat{p}(s)$, $\tau = 10$ ms.

networks increases exponentially, and this increase is τ invariant. The largest increase occurs between DIV14 and DIV18, a period when neuronal networks typically stabilize their activity, but these networks exhibit a rapid rate of dissipation. The entropies for both *APOE-KO-E2* and *APOE-KO-E4* networks are nearly constant from DIV10 to DIV18 for both $\tau = 10$ and 100 ms. The *APOE2* networks show a similar behavior throughout their development for $\tau = 10$ and 100 ms, with a small increase during development when $\tau = 3$ ms. These behaviors are independent of changes in the number of active electrodes over DIV; the respective figures for \bar{m} as seen in Figs. 13 and 14 in Appendix E have trends consistent with the ones describe above.

IV. DISCUSSION

We developed an analytical framework based on Shannon entropy to estimate mean entropy as a function of time in *in vitro* neuronal networks. We applied this framework to investigate early stage differences in network development of spontaneous voltage transients recorded from *in vitro* mouse neural-astrocyte hippocampal networks. The networks consisted of either neurons harvested from *APOE* knock out mice with exogenous astrocytes from *APOE2* or *APOE4* mice or cocultures of hippocampal and astrocytic cells from either *APOE2* or *APOE4* mice. Coordinated spontaneous neural activity provides the basis for the creation of healthy neural circuitry. The tools we developed allow us to quantify qualitative features observed in the rastergrams of network activity and to articulate dynamics that might not be easily visualized. Importantly, we use these tools to investigate whether early abnormalities in network development could forecast problems known to manifest later in life.

The framework assumes that neuronal networks are physical systems moving between energetic macrostates, where energy is defined as the number of channels that detect at

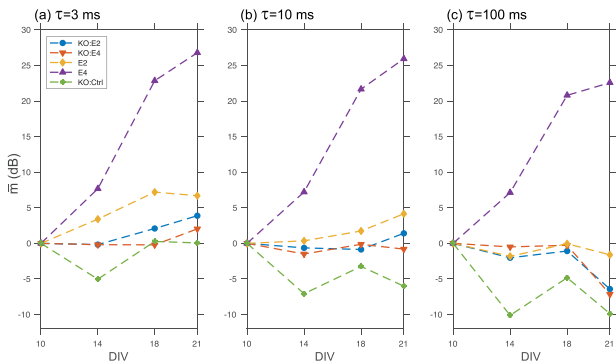


FIG. 9. Mean relative entropies for $\tau = 3, 10, 100$ ms. *APOE4* networks display an exponential increase in entropy during development, whereas the entropy for the *APOE-KO* control networks decrease exponentially; these effects are independent of τ . The fluctuations for the *APOE2* networks are small when $\tau = 10, 100$ ms and when $\tau = 3$ ms, there is a small increase over time. The *APOE-KO-E2* and *APOE-KO-E4* entropies are virtually constant from DIV10 until DIV18 for both $\tau = 10$ and 100 ms.

least one spike within a given bin. As such, each bin assumes the binary value of 0 or 1. We selected a range of bin sizes for our analyses that is within the physiologically relevant time frame for spiking activity and allows us to assess the stability of the calculated trends. The goal was to create a set of tools that are “tau-agnostic” within a physiological range. Furthermore, τ describes the resolution timescale with which we look at the networks; as we vary τ we adjust the zoom on our “temporal camera” and evaluate its impact on the calculated differences between the different treatments. In addition, we identify the existence of τ -invariant features that might mark stronger trends by fitting the probability distributions of energetic macrostates of networks to capture their collective developmental trend. The use of the generalized decreasing sigmoid best represents several features of the data: the quasi-linear decay at low energies, the plateau at median energies, and the final downward tail at high energies. We remark that the prevalence of the sigmoid function in quantifying evolutionary biological processes [61–63] might suggest the presence of a fundamental biological phenomenon observed in these current studies.

Out of all the energetic macrostates, the quiescent state ($e = 0$) is the most probable and this was observed for all networks throughout their development. This high probability of quiescence suggests that synchronous activity need not always lead to an increase in network activity. Rather, synchronicity can emerge due to a reorganization of the existing activity and these connections strengthen as the networks become more established over time. We propose a link to the high quiescent state probability to a physiological phenomena: the finite neurotransmitter available at each synapse during a spiking event. Repetitive firing at any given synapse will deplete neurotransmitter from synaptic vesicles and a delay will ensue to recycle “spent” vesicles [64,65].

The energy gradient maps with bright red regions, high probability density, and negative gradient suggest that the networks function as negative feedback loops. The higher the energy, the less probable it is for the energy to increase, presumably due to the reduced availability of neurotransmitter. The region defined by the slender green-blue arch relates to findings from neuronal avalanche studies [66,67]. The probability distribution in this region suggests that bursting is not a sharp, discrete event but it is preceded by a build up of spikes, akin to a neuronal avalanche. Our gradient maps show that the probability of moving directly from the quiescent state to a high energy state is very small; the networks must move along several paths with finite probability, leading to high energy states and these paths must pass through intermediate areas of increasingly energetic states. Lastly, there are high-probability transitions to lower energy states and these transitions are interspersed with large regions of zero probability. This pattern appears in all networks and is prominent later in development. It is most prominent in the *APOE-KO-E2* and *APOE2* networks, suggesting that as those networks mature, transitions from high energy states are restricted to discrete gradients and several transitions in the phase space are not accessible.

As previously stated, current state-of-the-art techniques do not allow for the direct measurement of network-wide information transmission. The MEA system measures the rate of change of the extracellular voltage, dV/dt , defined by the su-

perposition of the extracellular membrane potentials from any cell capacitively coupled to a channel. This is in contrast to an intracellular probe where the voltage, $V(t)$, is measured and arises due to the gating of ions through primarily membrane sodium and potassium channels. The approach that we have taken to define the entropy of the network is similar to the physical approach encountered in engineering thermodynamics where the rate of change of entropy, dS , is often divided into two separate components: $d_{\text{ext}}S$, due to external exchange of heat, and $d_{\text{int}}S$ due to the internal generation of entropy.

As such, we can write

$$dS = d_{\text{int}}S + d_{\text{ext}}S, \quad (19)$$

and since our system consists of an array of extracellular electrodes, we access the entropic rate component due to fluctuations in the external electromagnetic field.

There is a flattening of the entropy distribution for the networks containing *APOE-KO* neurons, and the distribution spans a broad range of energies for each network, regardless of the type of added astrocyte. These flat entropy distributions suggest the lack of a preference for a particular energetic state as it relates to transmission of information. The stable profile of the *APOE2* networks across all DIVs, with a peak around low energies, suggests a stable information transmission structure throughout their development. In contrast, the narrow range of the profile of *APOE4* networks suggests that information transmission capabilities of these networks might not be as robust.

The absence of APOE presents itself as a pathological neurological state with physiological deficits, and *APOE-KO* mice are used as a disease model [68–71]. However, while the *APOE4* allele is a *risk factor* for Alzheimer’s, *APOE4* mice are *not* a disease model. Importantly, neurological deficits attributed to the *APOE4* allele do not materialize until much later in life. As such, we were interested in investigating whether our measure might uncover unique dynamical irregularities early in network development. Indeed, our measure elucidates time-dependent changes in the mean entropy for all treatments, with the networks without APOE displaying a large attenuation. It may be that effective connections might not form during the development of these networks. It has been suggested that APOE is involved in synaptic transmission [50] and therefore a lack of APOE might adversely influence formation of healthy synapses. Adding astrocytes containing APOE—of either allele—arrests this deficiency, with reduced fluctuations over time. This suggests that APOE can facilitate the development of a healthy network state.

In contrast, the *APOE4* networks display an alarming trend in their mean entropy in the form of a dramatic, exponential increase in slope over time. As a result, these networks might be more sensitive to external perturbations. In fact, studies have shown that adult *APOE4* mice have a higher likelihood for seizure [72] as well as morphological abnormalities in their dendritic spines [73]. We record network activity during a pivotal period of development; neuronal networks are experiencing rapid creation and pruning of synapses to establish proper contacts, and we hypothesize that *APOE4* networks may be impaired in these efforts. Interestingly, while the *APOE2* networks have a slightly larger mean entropy than the *APOE-KO-E2* or *APOE-KO-E4* networks, in the case when

$\tau = 10$ and 100 ms, *APOE2* networks have reduced variability over time. These small fluctuations suggest that their information retention is stable during development.

We conclude by noting that these networks are created from *in vitro*, rather than *in vivo* preparations, making a clear one-to-one mapping to the brain dynamics less tenable. However, a major advantage to the coupling of an MEA system to cultured neuronal networks is the ability to uncover novel, time-dependent trends that are difficult, if not impossible, to currently measure *in vivo*. While results from these studies might be relevant to the fabrication of neuromorphic devices [74,75], conclusive, physiological studies are required to elucidate biochemical mechanisms. Here, we suggest, from a dynamics perspective, that *APOE2* networks operate within a steady state of information transmission during development. Additionally, we show that an unstable state is restored to a steady state when APOE-deficient networks are supplemented with exogenous APOE. Finally, in *APOE4* networks, where physiological deficits will not present themselves until later in life, our measure shows a propensity for instability that might serve as a harbinger of things to come.

ACKNOWLEDGMENTS

We thank Edoardo DeBenedetti for his insights into the regularization aspects of curve fitting, and broader intellectual discussions. This research was supported by the National Science Foundation (PHY-1205919 and IOS-1755033).

APPENDIX A: CELL CULTURE

Colonies of human *APOE2* and *APOE4* targeted replacement mice were bred in-house on a C57Bl6/J mouse background. These mice, homozygous for the *APOE2* or *APOE4* alleles, respectively, feature a targeted replacement of the murine *APOE* gene with human *APOE*. Expression of human *APOE* is driven by the endogenous murine promoter [76]. In addition, colonies of *APOE-KO* mice were bred in-house on a C57Bl6/J mouse background. To prepare individual embryonic (E17.5) hippocampal cultures from *APOE2*, *APOE4*, or *APOE-KO* mice, we used a protocol modified from [77]. Embryonic hippocampi were extracted into ice-cold dissection solution. The meninges were carefully removed from extracted tissue and the hippocampal tissue were finely chopped and digested with 0.1% trypsin followed by mechanical trituration. Before plating, MEA plates (MEA2100, Multi Channel Systems MCS GmbH, Reutlingen, Germany) were cleaned, autoclaved, and treated with poly-D-lysine and laminin (Sigma Aldrich, St. Louis, MO). A single cell suspension resulted from the trituration, and cells were added to the MEAs to achieve an approximate density of 700 cells/mm². At this plating density, spontaneous electrical activity was observed as early as DIV7 [78]. MEAs were covered with a gas permeable Teflon membrane to prevent evaporation of the media and to avoid contamination [79]. Cultures were maintained in Neuralbasal A supplemented with B27, penicillin/streptomycin, and horse serum (Thermo Fisher Scientific, Waltham, MA) in a humidified 5% CO₂ and 95% O₂ incubator at 37°C.

TABLE I. Number of experiments per treatment.

	DIV10	DIV14	DIV18	DIV21
<i>APOE2</i>	8	8	8	8
<i>APOE4</i>	8	8	8	8
<i>APOE-KO-E2</i>	16	16	15	15
<i>APOE-KO-E4</i>	13	13	13	13
<i>APOE-KO</i>	12	12	11	11

Table I shows the number of MEAs used for each treatment. Assuming normality, this setup yields $\text{Var}(\bar{m}) < 1\%$, 3%, 5% for $\tau = 3, 10, 100$ ms.

We see from Fig. 10 that the sample distributions of $\hat{p}(s)$ are comparable across treatments.

APPENDIX B: FINITE SAMPLE SIZE EFFECTS

Estimating information theoretic quantities has been a vibrant area of research in psychology, neurophysiology, and neuroscience. Most recently, Valiant and Valiant [80] introduced an algorithm that approaches this problem by finding the *simplest* histogram with the most similar fingerprint to that of the data. They compare it to the most common entropy estimators: the naive estimator \hat{H}_{MLE} [81,82] the Miller-Madow corrected estimator \hat{H}_{MM} [59], the jackknifed estimator \hat{H}_{JK} [83,84], the *best upper bound* estimator \hat{H}_{BUB} [85], and the Coverage Adjusted Estimator (CAE) [86].

Here, we show in Fig. 6 that the average $\hat{p}(0) \gtrsim 90\%$ and 80% for $\tau = 3$ and 10 ms, respectively. Furthermore, rare energetic states bring little contribution to i_τ . Considering the worst case scenario of $n_s = 1$, this accounts for $\tau/300 = 0.001\%$, 0.003% , and 0.03% for $\tau = 3, 10$, and 100 ms, respectively.

Table II shows that it is reasonable to use the Miller-Madow bias correction for $\tau = 3$ ms because $N_0/m_0 \gg 100$ and $N_1/m_1 \sim 100$, as pointed out by Paninski in [85]. Therefore, for consistency, we use the same estimator for $\tau = 10, 100$ ms.

We remark that, while recording for longer epochs might initially seem to solve to these limitations, these are living, evolving networks and it is important to consider the nonstationarity of developmental neuronal network activity. Indeed, we record for epochs that are short compared to the total lifetime of each network to assume stationarity; changes calculated during these epochs are assumed to be free of developmental effects. Considering the worst case scenario of $n_s = 1$ during a recording of 300 s under the stationarity assumption, obtaining 100 data points from which to estimate entropy would require a recording epoch of 500 min to ~ 8.3 h. This would adversely impact the health of the cells and, importantly, exceed the duration over which to assume stationarity.

APPENDIX C: OUTLIERS REMOVAL FOR ENERGY AND ENTROPY DISTRIBUTION FITS

Outliers were removed that did not satisfy an n -nearest-neighbors criterion before fitting commenced. In this study we selected $n = 2$ in order to eliminate pairs of isolated points.

TABLE II. Average sum $\widehat{p}_0 + \widehat{p}_1$, where $\widehat{p}_j \equiv \widehat{p}(1/N_{\text{active}})$ and the average ratios $N_0/m_0, N_1/m_1$, where $N_j = \widehat{p}_j N_\tau, m_j = N_{\text{active}} + j$, for $\tau = 3$ ms.

	DIV10			DIV14			DIV18			DIV21		
	$\widehat{p}_0 + \widehat{p}_1$	$\frac{N_0}{m_0}$	$\frac{N_1}{m_1}$	$\widehat{p}_0 + \widehat{p}_1$	$\frac{N_0}{m_0}$	$\frac{N_1}{m_1}$	$\widehat{p}_0 + \widehat{p}_1$	$\frac{N_0}{m_0}$	$\frac{N_1}{m_1}$	$\widehat{p}_0 + \widehat{p}_1$	$\frac{N_0}{m_0}$	$\frac{N_1}{m_1}$
<i>APOE2</i>	99%	2400	95	98%	2800	115	97%	2800	145	96%	2500	130
<i>APOE4</i>	99%	3300	60	99%	4800	100	99%	6500	210	99%	1600	245
<i>APOE-KO-E2</i>	97%	2000	115	96%	1700	95	93%	1600	78	92%	1500	70
<i>APOE-KO-E4</i>	97%	2000	105	95%	1700	85	93%	1600	75	93%	1600	70
<i>APOE-KO</i>	99%	4100	118	98%	2700	90	95%	2400	90	95%	2200	65

We define the threshold vector $\mathbf{R} = (r_1, r_2)$, where r_i is the threshold radius for the i th closest neighbor.

$$r_i = \mu_i + \sigma_i, \quad (\text{C1})$$

where μ_i and σ_i , respectively, are the mean value and the standard deviation of the distance of the i th closest neighbor.

For every data point j we defined the closest-neighbors vector $\mathbf{D}_j = (d_1, d_2)$, where d_i is the distance from the i th closest neighbor.

The test condition is

$$\text{test}_j = \begin{cases} 0, & \text{if } \min(\mathbf{D}_j - \mathbf{R}) > 0 \\ 1, & \text{otherwise,} \end{cases} \quad (\text{C2})$$

and we removed all the data points for which $\text{test}_j = 0$, that is, we removed all the data points that do not show at least 1 nearest neighbor within their threshold radius.

APPENDIX D: OUTLIERS REMOVAL FOR MEAN ENTROPY FITS

To evaluate changes in the mean relative entropy, \overline{m} , we omitted those values that fall outside of a $\pm 1\sigma$ interval around the initial mean value μ_m .

APPENDIX E: SUPPLEMENTAL FIGURES

This Appendix contains supplementary figures for completeness of the analysis described in the main body.

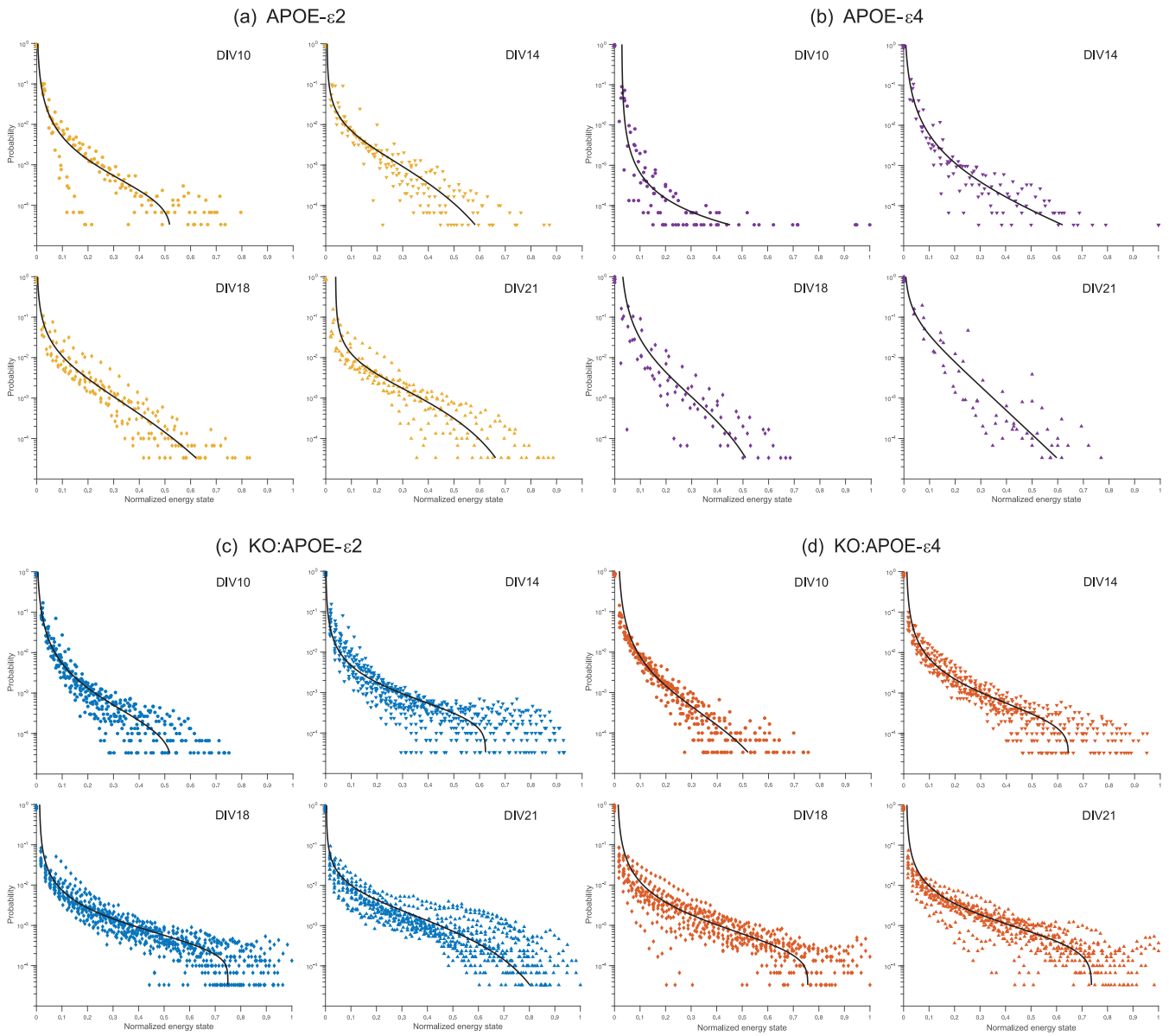


FIG. 11. Raw superimposed probability distributions over DIV for $\tau = 10$ ms, with sigmoid fits.

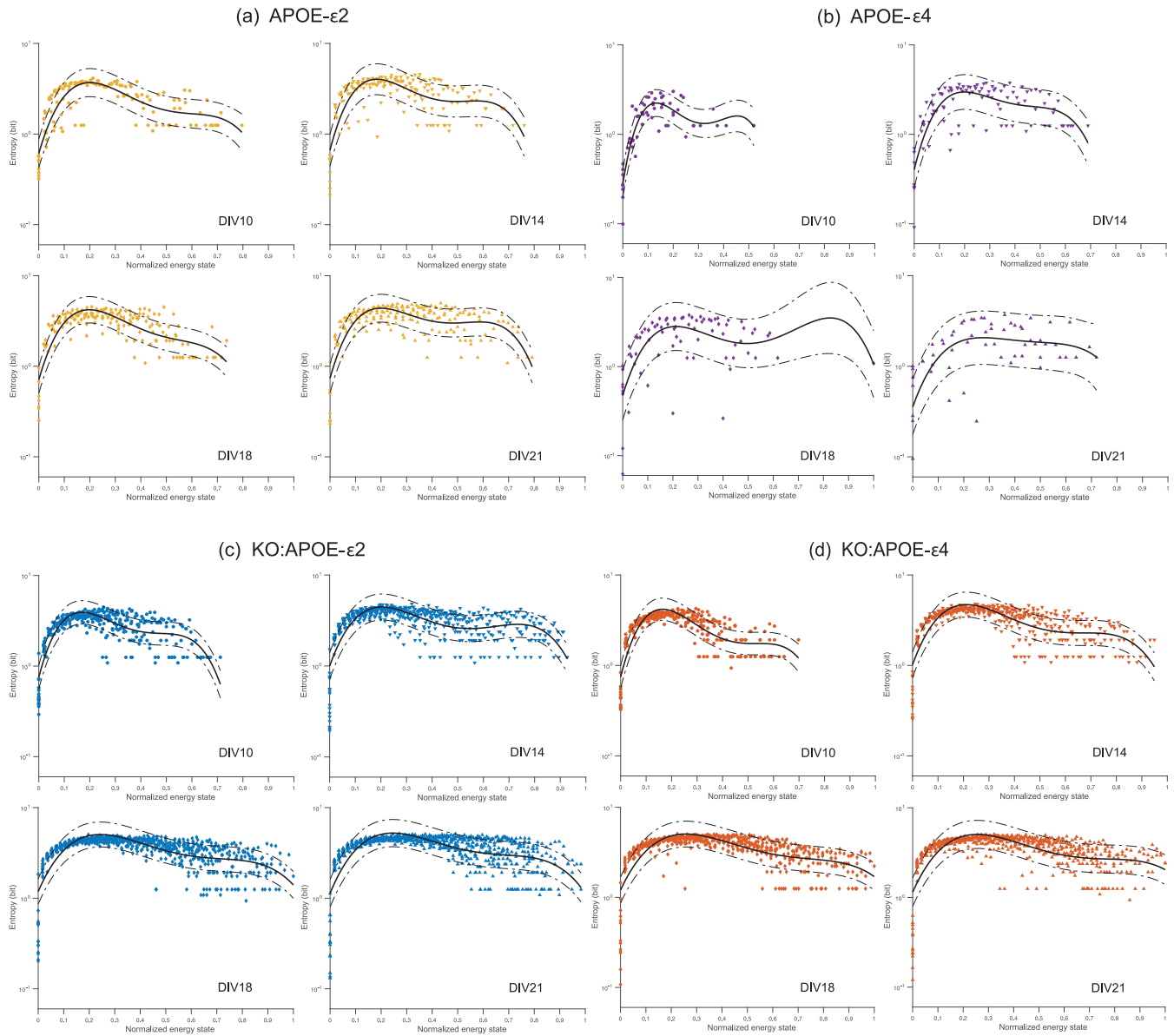


FIG. 12. Raw superimposed entropy distributions over DIV for $\tau = 10$ ms, with fourth degree polynomial and a confidence region greater than 50%. Entropy is measured in bits and its physical interpretation is the amount of information that a network discharges based on its energy state. Initially, on DIV10, all networks display a similar peak near the energy state $e \sim 0.2$. The $e \sim 0.2$ peak and general profile for the *APOE2* networks is nearly constant throughout the development of those networks. *APOE-KO-E2* and *APOE-KO-E4* networks broaden their profiles over time, with their maximum entropies flattening as the networks develop. The changes in energy do not result in changes in entropy, indicating the presence of a white noiselike entropy distribution. The peak in the *APOE4* networks flattens over development with a rightward shift.

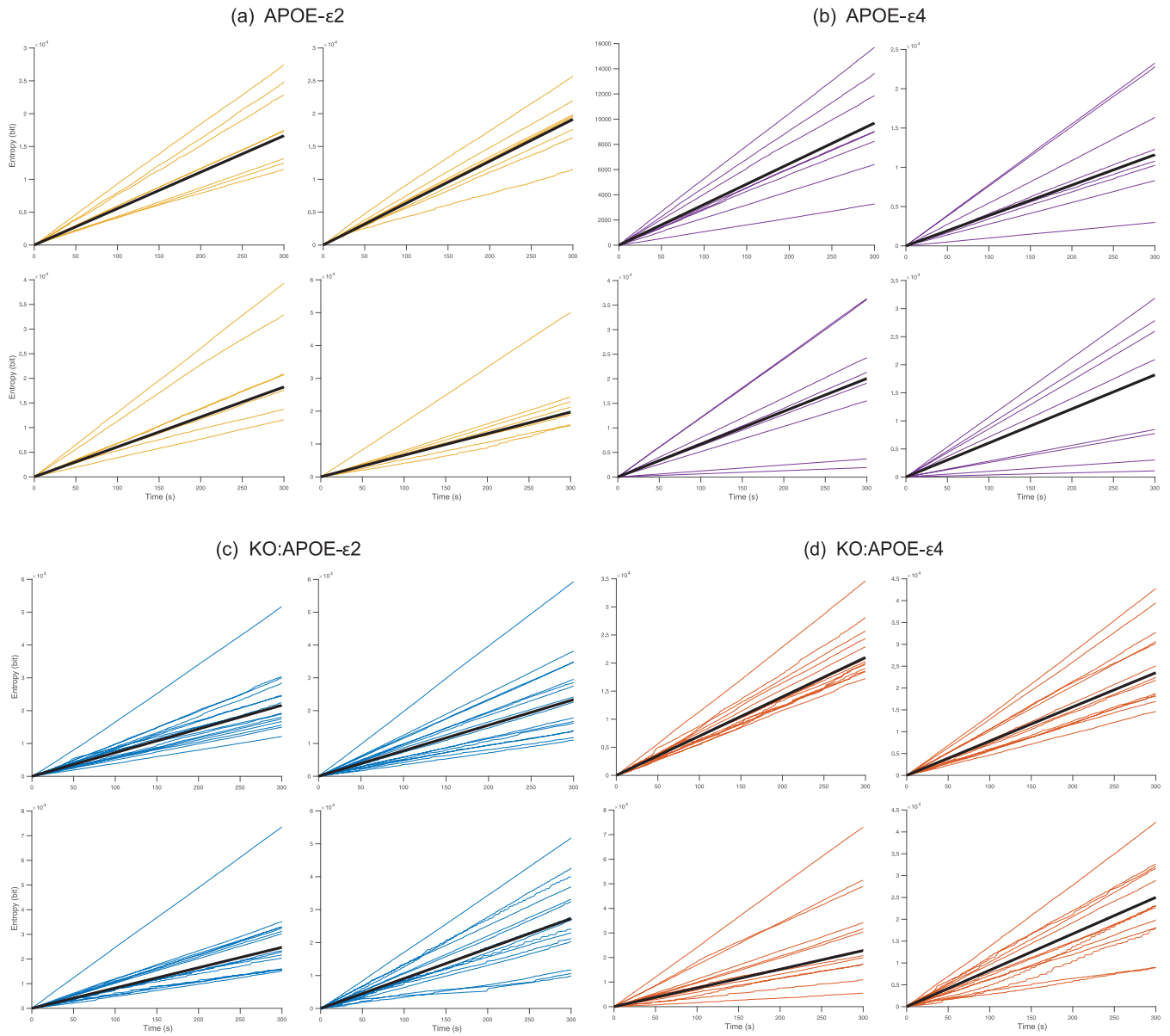


FIG. 13. Raw superimposed cumulative entropies over time, over DIV, for $\tau = 100$ ms, with linear fit.

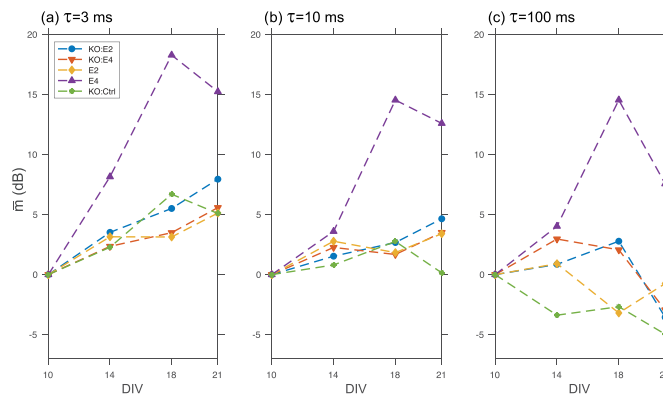


FIG. 14. Mean relative entropies over DIV, for all values of τ .

- [1] D. Attwell and S. B. Laughlin, An energy budget for signaling in the grey matter of the brain, *J. Cereb. Blood Flow Metab.* **21**, 1133 (2001).
- [2] J. J. Harris and D. Attwell, The energetics of CNS white matter, *J. Neurosci.* **32**, 356 (2012).
- [3] A. J. Smith, H. Blumenfeld, K. L. Behar, D. L. Rothman, R. G. Shulman, and F. Hyder, Cerebral energetics and spiking frequency: The neurophysiological basis of fMRI, *Proc. Natl. Acad. Sci. U.S.A.* **99**, 10765 (2002).
- [4] L. Yu and Y. Yu, Energy-efficient neural information processing in individual neurons and neuronal networks, *J. Neurosci. Res.* **95**, 2253 (2017).
- [5] M. Bélanger, I. Allaman, and P. J. Magistretti, Brain energy metabolism: Focus on Astrocyte-neuron metabolic cooperation, *Cell Metab.* **14**, 724 (2011).
- [6] J. W. Deitmer, S. M. Theparambil, I. Ruminot, S. I. Noor, and H. M. Becker, Energy dynamics in the brain: Contributions of astrocytes to metabolism and pH homeostasis, *Front. Neurosci.* **13**, 1301 (2019).
- [7] M. Santello, N. Toni, and A. Volterra, Astrocyte function from information processing to cognition and cognitive impairment (2019).
- [8] L. F. Abbott, *Zoology* (Elsevier GmbH, Netherlands, 2003), Vol. 106, pp. 365–371.
- [9] G. G. Turrigiano and S. B. Nelson, Homeostatic plasticity in the developing nervous system (2004).
- [10] G. Turrigiano, Homeostatic synaptic plasticity: Local and global mechanisms for stabilizing neuronal function, *Cold Spring Harb. Perspec. Biol.* **4** (2012).
- [11] G. W. Davis, Homeostatic signaling and the stabilization of neural function (2013).
- [12] W. Wefelmeyer, C. J. Puhl, and J. Burrone, Homeostatic plasticity of subcellular neuronal structures: From inputs to outputs (2016).
- [13] N. W. Tien and D. Kerschensteiner, Homeostatic plasticity in neural development (2018).
- [14] Y. Ben-Ari, Developing networks play a similar melody, *Trends Neurosci.* **24**, 353 (2001).
- [15] A. G. Blankenship and M. B. Feller, Mechanisms underlying spontaneous patterned activity in developing neural circuits (2010).
- [16] L. A. Kirkby, G. S. Sack, A. Firl, and M. B. Feller, A role for correlated spontaneous activity in the assembly of neural circuits (2013).
- [17] M. J. Chacron, A. Longtin, and L. Maler, *Netw., Comput. Neural Syst.* **14**, 803 (2003).
- [18] M. B. Feller, Spontaneous correlated activity in developing neural circuits (1999).
- [19] M. J. Chacron, A. Longtin, and L. Maler, Negative interspike interval correlations increase the neuronal capacity for encoding time-dependent stimuli, *J. Neurosci.* **21**, 5328 (2001).
- [20] M. J. Chacron, A. Andr', A. Longtin, and L. Maler, *J. Comput. Neurosci.*, (2004).
- [21] C. Gonzalez-Islas and P. Wenner, Spontaneous network activity in the embryonic spinal cord regulates AMPAergic and GABAergic synaptic strength, *Neuron* **49**, 563 (2006).
- [22] J. Tabak, M. Mascagni, and R. Bertram, Mechanism for the universal pattern of activity in developing neuronal networks, *J. Neurophysiol.* **103**, 2208 (2010).
- [23] S. B. Laughlin, Energy as a constraint on the coding and processing of sensory information (2001).
- [24] J. Barral and A. Reyes, Optogenetic stimulation and recording of primary cultured neurons with spatiotemporal control, *Bio-Protoc.* **7**, e2335 (2017).
- [25] T. V. P. Bliss and T. Lomo, Long-lasting potentiation of synaptic transmission in the dentate area of the anaesthetized rabbit following stimulation of the perforant path, *J. Physiol.* **232**, 331 (1973).
- [26] R. C. Malenka and R. A. Nicoll, Long-term potentiation—A decade of progress? *Science* **285**, 1870 (1999).
- [27] E. Molnár, Long-term potentiation in cultured hippocampal neurons (2011).
- [28] R. A. Nicoll, A brief history of long-term potentiation (2017).
- [29] M. Abeles, Y. Prut, H. Bergman, and E. Vaadia, *Progress in Brain Research.*
- [30] G. Buzsáki and A. Draguhn, Neuronal oscillations in cortical networks, *Science* **304**, 1926 (2004).
- [31] L. L. Colgin, T. Denninger, M. Fyhn, T. Hafting, T. Bonnevie, O. Jensen, M. B. Moser, and E. I. Moser, Frequency of gamma oscillations routes flow of information in the hippocampus, *Nature (London)* **462**, 353 (2009).
- [32] F. Montani, R. A. Ince, R. Senatore, E. Arabzadeh, M. E. Diamond, and S. Panzeri, The impact of high-order interactions on the rate of synchronous discharge and information transmission in somatosensory cortex, *Philos. Trans. R. Soc. A* **367**, 3297 (2009).
- [33] E. T. Rolls, T. J. Webb, and G. Deco, Communication before coherence, *Eur. J. Neurosci.* **36**, 2689 (2012).
- [34] C. C. Canavier, Phase-resetting as a tool of information transmission (2015).
- [35] G. Hahn, A. Ponce-Alvarez, G. Deco, A. Aertsen, and A. Kumar, Portraits of communication in neuronal networks (2019).
- [36] A. Borst and F. E. Theunissen, Information theory and neural coding, *Nat. Neurosci.* **2**, 947 (1999).
- [37] S. Panzeri, S. R. Schultz, A. Treves, and E. T. Rolls, Correlations and the encoding of information in the nervous system, *Proc. R. Soc. B* **266**, 1001 (1999).
- [38] K. Kang and H. Sompolinsky, Mutual Information of Population Codes and Distance Measures in Probability Space, *Phys. Rev. Lett.* **86**, 4958 (2001).
- [39] M. N. Safran, V. L. Flanagan, A. Borst, and H. Sompolinsky, Adaptation and information transmission in fly motion detection, *J. Neurophysiol.* **98**, 3309 (2007).
- [40] J. D. Fitzgerald and T. O. Sharpee, Maximally informative pairwise interactions in networks, *Phys. Rev. E* **80**, 031914 (2009).
- [41] A. Fairhall, E. Shea-Brown, and A. Barreiro, Information theoretic approaches to understanding circuit function (2012).
- [42] L. Meshulam, J. L. Gauthier, C. D. Brody, D. W. Tank, and W. Bialek, Collective behavior of place and non-place neurons in the hippocampal network, *Neuron* **96**, 1178 (2017).
- [43] O. Ozan Koyluoglu, Y. Pertzov, S. Manohar, M. Husain, and I. R. Fiete, Fundamental bound on the persistence and capacity of short-term memory stored as graded persistent activity, *eLife* **6**, e22225 (2017).
- [44] R. E. Kass, S.-I. Amari, K. Arai, E. N. Brown, C. O. Diekmann, M. Diesmann, B. Doiron, U. T. Eden, A. L. Fairhall, G. M. Fiddymant *et al.*, Computational neuroscience: Mathematical and statistical perspectives, *Ann. Rev. Stat. Appl.* **5**, 183 (2018).

- [45] B. Paprocki, A. Pregowska, and J. Szczepanski, *Bull. Pol. Acad. Sci.: Tech. Sci.* **68**, 225 (2020).
- [46] L. Montangie and F. Montani, Effect of interacting second- and third-order stimulus-dependent correlations on population-coding asymmetries, *Phys. Rev. E* **94**, 042303 (2016).
- [47] M. Griguoli and E. Cherubini, Early correlated network activity in the hippocampus: Its putative role in shaping neuronal circuits (2017).
- [48] C. C. Liu, T. Kanekiyo, H. Xu, and G. Bu, Apolipoprotein e and Alzheimer disease: Risk, mechanisms and therapy (2013).
- [49] N. Zhao, C. C. Liu, W. Qiao, and G. Bu, Apolipoprotein E, receptors, and modulation of Alzheimer's disease, *Biol. Psychiatry* **83**, 347 (2018).
- [50] D. M. Holtzman, J. Herz, and G. Bu, Apolipoprotein E and apolipoprotein E receptors: Normal biology and roles in Alzheimer Disease, *Cold Spring Harb. Perspect. Medicine* **2**, a006312 (2012).
- [51] Y. Huang and R. W. Mahley, Apolipoprotein E: Structure and function in lipid metabolism, neurobiology, and Alzheimer's diseases, *Neurobiol. Dis.* **72**, 3 (2014).
- [52] M. Chen, M. Xie, C. Peng, and S. Long, The absorption of apolipoprotein E by damaged neurons facilitates neuronal repair, *Cell Biol. Int.* **43**, 623 (2019).
- [53] E. H. Corder, A. M. Saunders, N. J. Risch, W. J. Strittmatter, D. E. Schmechel, P. C. Gaskell, J. B. Rimmler, P. A. Locke, P. M. Conneally, K. E. Schmechel *et al.*, Protective effect of apolipoprotein E type 2 allele for late onset Alzheimer disease, *Nat. Genet.* **7**, 180 (1994).
- [54] Z. Zhu, R. Wang, and F. Zhu, The energy coding of a structural neural network based on the Hodgkin-Huxley model, *Front. Neurosci.* **12**, 122 (2018).
- [55] MATLAB, MATLAB release 2020a (2020).
- [56] MATLAB, Optimization Toolbox (2006).
- [57] T. F. Coleman and Y. Li, An interior trust region approach for nonlinear minimization subject to bounds, *SIAM J. Optim.* **6**, 418 (1996).
- [58] T. F. Coleman and Y. Li, On the convergence of interior-reflective Newton methods for nonlinear minimization subject to bounds, *Math. Program.* **67**, 189 (1994).
- [59] G. A. Miller, *Inf. Theory Psychol.: Prob. Methods* **2**, 95 (1955).
- [60] C. E. Shannon, A mathematical theory of communication, *Bell Syst. Tech. J.* **27**, 623 (1948).
- [61] F. J. Richards, A flexible growth function for empirical use, *J. Exp. Bot.* **10**, 290 (1959).
- [62] F. Kozusko and M. Bourdeau, A unified model of sigmoidal tumour growth based on cell proliferation and quiescence, *Cell Proliferation* **40**, 824 (2007).
- [63] T. Mäkelä and A. Annala, Natural patterns of energy dispersal, *Phys. Life Rev.* **7**, 477 (2010).
- [64] R. S. Zucker and W. G. Regehr, Short-term synaptic plasticity, *Annu. Rev. Physiol.* **64**, 355 (2002).
- [65] L. F. Abbott and W. G. Regehr, Synaptic computation, *Nature (London)* **431**, 796 (2004).
- [66] J. M. Beggs and D. Plenz, Behavioral/systems/cognitive neuronal avalanches in neocortical circuits, *J. Neurosci.* **23**, 11167 (2003).
- [67] J. M. Beggs and D. Plenz, Neuronal avalanches are diverse and precise activity patterns that are stable for many hours in cortical slice cultures, *J. Neurosci.* **24**, 5216 (2004).
- [68] H. Shimano, J. Ohsuga, M. Shimada, Y. Namba, T. Gotoda, K. Harada, M. Katsuki, Y. Yazaki, and N. Yamada, Inhibition of diet-induced atheroma formation in transgenic mice expressing apolipoprotein E in the arterial wall, *J. Clin. Invest.* **95**, 469 (1995).
- [69] S. H. Zhang, R. L. Reddick, J. A. Piedrahita, and N. Maeda, Spontaneous hypercholesterolemia and arterial lesions in mice lacking apolipoprotein E, *Science* **258**, 468 (1992).
- [70] G. Ghiselli, E. Schaefer, P. Gascon, and H. Breser, Type III hyperlipoproteinemia associated with apolipoprotein E deficiency, *Science* **214**, 1239 (1981).
- [71] I. F. Tudorache, V. G. Trusca, and A. V. Gafencu, Apolipoprotein E—A multifunctional protein with implications in various pathologies as a result of its structural features, *Comput. Struct. Biotechnol.* **15**, 359 (2017).
- [72] J. M. Hunter, J. R. Cirrito, J. L. Restivo, R. D. Kinley, P. M. Sullivan, D. M. Holtzman, D. Koger, C. Delong, S. Lin, L. Zhao *et al.*, Emergence of a seizure phenotype in aged apolipoprotein epsilon 4 targeted replacement mice, *Brain Res.* **1467**, 120 (2012).
- [73] G. A. Rodriguez, M. P. Burns, E. J. Weeber, and G. W. Rebeck, Young APOE₄ targeted replacement mice exhibit poor spatial learning and memory, with reduced dendritic spine density in the medial entorhinal cortex, *Learn. Mem.* **20**, 256 (2013).
- [74] R. George, M. Chiappalone, M. Giugliano, T. Levi, S. Vassanelli, J. Partzsch, and C. Mayr, Plasticity and adaptation in neuromorphic biohybrid systems, *iScience* **23**, 101589 (2020).
- [75] S. Nazari, K. Faez, M. Amiri, and E. Karami, A digital implementation of neuron-astrocyte interaction for neuromorphic applications, *Neural Networks* **66**, 79 (2015).
- [76] P. M. Sullivan, H. Mezdour, Y. Aratani, C. Knouff, J. Najib, R. L. Reddick, S. H. Quarfordt, and N. Maeda, Targeted replacement of the mouse apolipoprotein E gene with the common human APOE3 allele enhances diet-induced hypercholesterolemia and atherosclerosis, *J Biol. Chem.* **272**, 17972 (1997).
- [77] D. T. S. Pak, S. Yang, S. Rudolph-Correia, E. Kim, and M. Sheng, *Neuron*, (2001).
- [78] M. Niedringhaus, X. Chen, R. Dzakupasu, and K. Conant, MMPs and soluble ICAM-5 increase neuronal excitability within in vitro networks of Hippocampal neurons, *PLoS One* **7**, e42631 (2012).
- [79] S. M. Potter and T. B. Demarse, A new approach to neural cell culture for long-term studies, *J. Neurosci. Methods* (2001).
- [80] G. Valiant and P. Valiant, Estimating the unseen: Improved estimators for entropy and other properties, *J. ACM* **64**, 37 (2017).
- [81] S. P. Strong, R. Koberle, R. R. d. R. van Steveninck, and W. Bialek, (1996).
- [82] A. Antos and I. Kontoyiannis, Convergence properties of functional estimates for discrete distributions, *Random Struct. Alg.* **19**, 163 (2001).
- [83] B. Efron and C. Stein, The Jackknife estimate of variance, *Ann. Statist.* **9**, 586 (1981).
- [84] S. Zahl, Jackknifing an index of diversity, *Ecology* **58**, 907 (1977).
- [85] L. Paninski, Estimation of entropy and mutual information, *Neural Comput.* **15**, 1191 (2003).
- [86] A. Chao and T.-J. Shen, Nonparametric estimation of Shannons index of diversity when there are unseen species in sample, *Environ. Ecol. Stat.* **10**, 429 (2003).